

Comparative Study of Tribological and Mechanical Properties Between Single Layers of Al_2O_3 and Si_3N_4 Deposited on AISI 316 Stainless Steel

E. Hernandez-Rengifo^{a,*}, C.H. Ortiz^a, C.H. Hidalgo^a, J.A. Ballesteros^a, J.C. Caicedo^a

^aTribology, Powder Metallurgy and Processing of Solid Recycled Research Group, Universidad del Valle, Cali Colombia.

Keywords:

Physical vapor deposition PVD
Mechanical properties
 Al_2O_3
 Si_3N_4
Lubricated tribological properties

* Corresponding author:

Erick Hernandez Rengifo 
E-mail:
Erick.hernandez@correounivalle.edu.co

Received: 1 September 2020
Revised: 12 October 2020
Accepted: 5 January 2021

ABSTRACT

Al_2O_3 and Si_3N_4 coatings have been extensively studied separately, showing excellent performance in resistance to corrosion and wear. In the present work, the structural, morphological, mechanical and tribological properties of Al_2O_3 and Si_3N_4 single-layer coatings deposited on AISI 316 stainless steel substrates were studied by means of the R. F. Magnetron Sputtering technique. By X-ray diffraction (XRD) The structures of the coatings were determined, the chemical composition was studied by X-ray Photoelectron Spectroscopy (XPS). By means of Atomic Force Microscopy (AFM) the grain size and roughness were analyzed, through Scanning Electron Microscopy (SEM) the wear surfaces produced by the Pin-On-Disk and the Scratch tests were studied. By nanoindentation technique the behavior in hardness and elastic modulus was evaluated, finding better performance in the Si_3N_4 coating. The friction coefficient was evaluated by Pin-On-Disk tests in dry and lubricated environments. The critical load against adhesive wear was determined for Al_2O_3 and for Si_3N_4 . This study develops a comparison between the mechanical and tribological properties of the mentioned coatings, proposing their possible application in components of the food and pharmaceutical industry that are subjected to phenomena where Al_2O_3 and Si_3N_4 coatings could mitigate.

© 2021 Published by Faculty of Engineering

1. INTRODUCTION

The food and pharmaceutical industry is an important sector in industrial development, it is constantly evolving due to the growing expectations of consumers, as well as the high biosafety protocols within its processes. The appearance of electrochemical and tribological

phenomena in processing equipment can affect the quality of products, components and their consumers, these phenomena are the main responsible for the loss of productivity and efficiency in these industries [1-3]. Due to this, new alternatives are being sought to generate greater reliability in equipment and its components. An option to this problem is the

implementation of protective coatings such as Al_2O_3 [4], Si_3N_4 [5], $(\text{CrN}/\text{Si}_3\text{N}_4)$ [6], TiO_2 [7], among others. These coatings have the ability to improve the mechanical, tribological and electrochemical properties of the coated devices, due to the fact that these coatings present a high resistance to corrosion, as well as a greater resistance to wear, providing a longer useful life of the components, which they influence the productivity of companies and the quality of their products [7]. Therefore, aluminum oxide (Al_2O_3) coatings are widely used in industrial processes due to its excellent properties, is mainly linked by ionic bonds, it has excellent chemical stability. Furthermore, it exhibits only a small loss of mechanical strength with increasing temperature. Therefore, under high temperature conditions (above 800°C), Al_2O_3 is the coating material that performs best in terms of hot hardness. Chemical inertness in combination with Al_2O_3 's electrical insulation, which is diffusion tight, results in superior oxidation resistance than average coatings. These characteristics of Al_2O_3 are also used in compounds that have AL such as TiAlN , among others. The ability of aluminum to form very thin, diffusion-proof Al_2O_3 reaction layers in an oxidizing atmosphere is the basis for alloying concepts in all high-temperature alloys that normally contain aluminum as an alloying element for protection against oxidation. Passive protective layers of Al_2O_3 are formed on the different coatings, making them considerably more resistant to oxidation than coatings without aluminum [8-10], is usually amorphous and it has good corrosion resistance. At a critical temperature of approximately 500°C , its density and ablation change [11]. On the other hand, silicon nitride (Si_3N_4) based coatings typically exhibit excellent heat resistance, good wear resistance, and high chemical stability, as well as good resistance to thermal shock and high temperatures (superior to Al_2O_3 cutting tools), and therefore They are both widely used in gray cast iron cutting and high speed dry machining of nickel-based alloys. However, during high-speed dry machining of Fe-based workpieces, Si_3N_4 cutting tools will react with Fe in the workpiece at high cutting temperatures, resulting in rapid tool wear. cutting edge, therefore, will seriously limit your applications [12,13]. These coatings have been evolving due to their excellent chemical,

mechanical and tribological properties, where their low coefficient of friction and chemical inertia to aggressive environments is important depending on the application [14,15]. As mentioned above, both coatings are candidates for use as protective coatings in industrial processes. The objective of this work consisted in the study of the behavior in the mechanical and tribological properties in a dry and lubricated environment of the Al_2O_3 and Si_3N_4 monolayer coatings deposited on AISI 316 stainless steel substrates, with the objective of correlating said results to determine which coating presents the best set of properties, being this the best option to be implemented as a protective coating in devices used in the food and pharmaceutical industry [14,15].

Taking into account the above criteria, several authors have tried to relate the physical properties of Al_2O_3 and Si_3N_4 coatings separately with the mechanical properties. Additionally, it is possible to find contributions to the physical mechanisms of Al_2O_3 and Si_3N_4 in the literature with the evolution of their mechanical properties. However, a comparative study of the mechanical and tribological properties of Al_2O_3 and Si_3N_4 single-layer coatings has not yet been fully explored.

2. EXPERIMENTAL SECTION

2.1 Deposition process

The deposition of the coatings was performed by the magnetron sputtering technique with an r.f. source (13.56 MHz) on silicon (100) and AISI 316 stainless steel substrates. Stoichiometric cathodes of Al_2O_3 and Si_3N_4 with a purity of 99.9% were used. Prior to the deposition process, the substrates were ultrasonically cleaned using isopropanol and acetone. During the deposition process a power of 450 W and 550 W was used for Al_2O_3 and Si_3N_4 , respectively, a bias voltage of -20V, a distance between substrate - cathode of 7 cm, and a temperature of 200°C was maintained inside the chamber. Also, the substrate holder rotated at a speed of 60 RPM during the whole process of deposition with a working pressure of 5.1×10^{-3} mbar. Both layers presented approximately $2.5\ \mu\text{m}$ thick.

2.2 Characterization technique for coatings

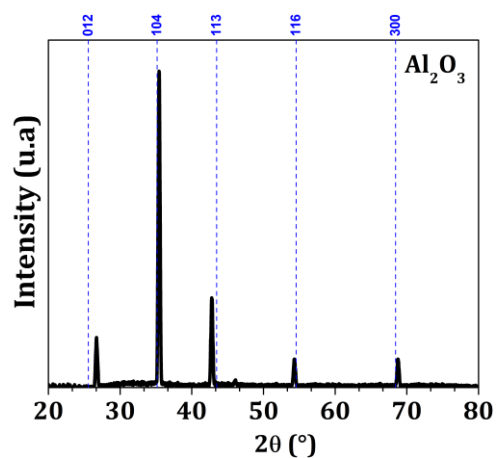
The structural characterization was performed by X-ray diffraction (XRD) using a PANalytical X'Per PRO diffractometer with Cu radiation $K\alpha$ ($\lambda = 1.5406 \text{ \AA}$) in Bragg-Brentano configuration ($\theta/2\theta$) at high angles, because the thickness of the coatings is 2.5 microns, the Bragg-Brentano configuration can be used, taking into account that they are deposited on monocrystalline silicon substrates and the coating is thick, there is no contribution from the substrate. The thicknesses were obtained by scanning electron microscopy (SEM) using the JSM 6490LV JEOL equipment in secondary electron mode. The chemical characterization and the types of bonds present in the coatings were studied by X-ray Photoelectronic Spectroscopy (XPS) through an ESCAPHI 5500 equipment with monochromatic Al- $K\alpha$ radiation and with energy step of 0.1 eV. By means of atomic force microscopy (AFM), roughness and grain size were measured using an Asylum Research MFP-3D® equipment and analyzed with the image processor (SPIP®). The mechanical properties such as hardness (H) and modulus of elasticity (E), also, the load-penetration curves of the surfaces were obtained by the nanoindentation technique using a Ubil-Hystron with a Berkovich type indenter with variable load. The tribological behavior of the Al_2O_3 and Si_3N_4 coatings were performed under the ASTM G99-17 [16] standard using a Microtest MT 4001-98 tribometer with a 6 mm diameter pin made of 100Cr6 steel as the reference counterpart, applying a 5 N load with a 300 m travel and 160 rpm angular speed. The lubricant used in this test was LUBRIPLATE FMO 85 AW, with applications in food and pharmaceutical processing, moreover in machinery. Finally, the scratch test technique was used under the ASTM G171-03 [17] standard with the Microtest MTR2 equipment, using a scratch distance of 6 mm with an increasing load of 0-90 N and a pitch of 1.97 mm/min; after that, a 3D topographic map of the wear tracks was made using a KLA Tencor D-120 profilometer.

3. RESULTS AND DISCUSSION

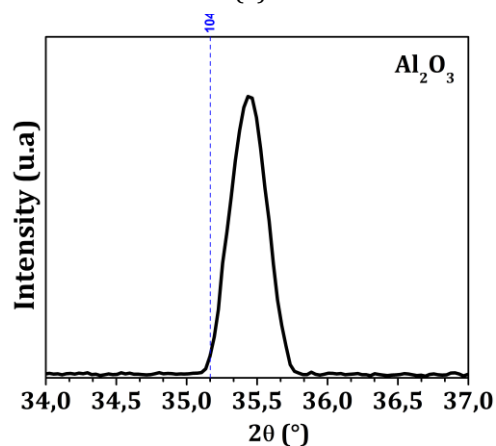
3.1 X-Ray diffraction (DRX)

Fig. 1. (a) and (c) shows the XRD diffraction patterns for the Al_2O_3 and Si_3N_4 systems

respectively deposited on silicon (100), where diffraction peaks were obtained located in the crystallographic planes (012), (104), (113), (116), (300) characteristic of a hexagonal structure belonging to Al_2O_3 and the planes (111), (220), (311), (400), (511), (440), (533) characteristic of a face centered cubic structure (FCC) belonging to Si_3N_4 . A preferential texturing of the crystals is observed in the direction (104) for Al_2O_3 and in the direction (311) for Si_3N_4 , respectively. The horizontal displacements at 2θ of the diffraction peaks with respect to those reported in the index cards JCPDC 00- 002-1373 for Al_2O_3 and (ICDD) 00-051-1334 for Si_3N_4 , were caused by internal stresses generated during the deposition process, which caused a deformation in the crystallographic planes of the coatings' structures. Fig. 1b and 1d show a maximum peak magnification for the Al_2O_3 and Si_3N_4 patterns. Therefore, it is possible to observe a shift towards higher values of the 2θ angle where the effect of the stresses generated by the interface between the substrate and the coating during the growth process of the coating is evident



(a)



(b)

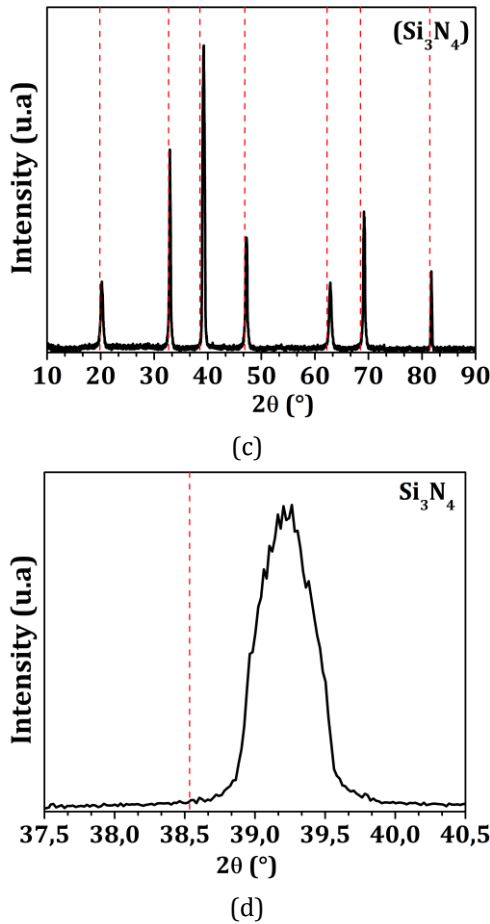


Fig. 1. Diffraction patterns of the single layers coating deposited on Silicon (a) Al₂O₃ coating patterns, (b) Al₂O₃ coating diffraction pattern magnification, (c) Si₃N₄ coating patterns, and (d) Si₃N₄ coating diffraction pattern magnification.

The presence of internal forces was observed through the lattice parameter a_0 , using Bragg's law (Eq.1) and the lattice parameter equation (Eq.2), because the Al₂O₃ coatings presented a hexagonal structure where the parameters $a_0 = b \neq c_0$ are found, and it is necessary to consider an expression that relates both parameters (Eq.3) [18,19].

$$n\lambda = 2d\sin\theta \tag{1}$$

$$d = \frac{a_0}{\sqrt{h^2 + k^2 + l^2}} \tag{2}$$

$$d = \frac{a_0}{\sqrt{\frac{4}{3}(h^2 + hk + k^2) + (l^2/c^2)}} \tag{3}$$

Where d is the interplanar distance, a_0 the lattice parameter y ($h.k.l$) are the miller indices and the diffraction angles come from the diffraction

patterns (Fig.1). By correlating the above equations it was possible to determine Eq.4 and Eq.5 for the FCC structure belonging to Si₃N₄ and the hexagonal structure belonging to Al₂O₃, respectively [19].

$$a_0 = \frac{n\lambda\sqrt{h^2 + k^2 + l^2}}{2d\sin\theta} \tag{4}$$

$$a_0 = \sqrt{\frac{4/3(h^2 + k^2 + l^2)}{\frac{(2\sin\theta)^2}{(n\lambda)^2} - \frac{l^2}{c^2}}} \tag{5}$$

Figure 2 presents the values of the network parameter for both layers obtained through the above equations. It was determined that both layers presented a decrease in said values, obtaining a decrease of 1.6% for Al₂O₃ and a decrease of 1.8% for Si₃N₄, indicating the presence of compressive stresses within the structures. These stresses are attributed to the atomic bombardment on the surface of the coating during the deposition process, which generated displacements of atoms from their equilibrium position through a series of collisions, producing a volumetric distortion. In addition, the diffusion of atoms or defects which are diffused within the grain boundary, generates a compression of the grains on both sides of the boundary producing compressive stresses in the structure [20].

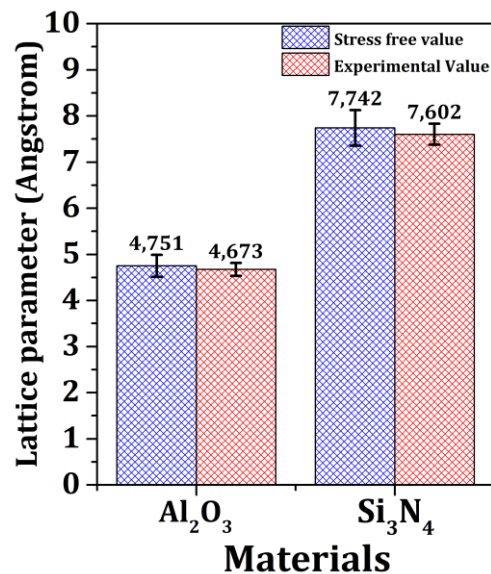


Fig. 2. Network parameter variation between the stress-free material and the Al₂O₃ and Si₃N₄ coatings deposited on Si (100) substrates.

3.2 Photoelectronic X-Ray spectroscopy (XPS)

Figs. 3a and 3b show the individual depth spectra for each coating, presenting the characteristic spectral lines of the elements present, using the X-ray photoelectron spectroscopy (XPS) technique for the Al_2O_3 and Si_3N_4 coatings, respectively.

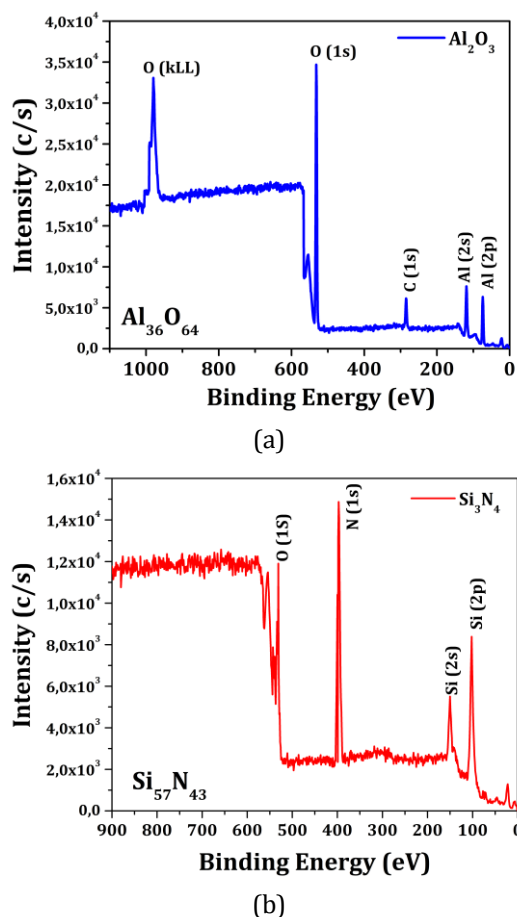
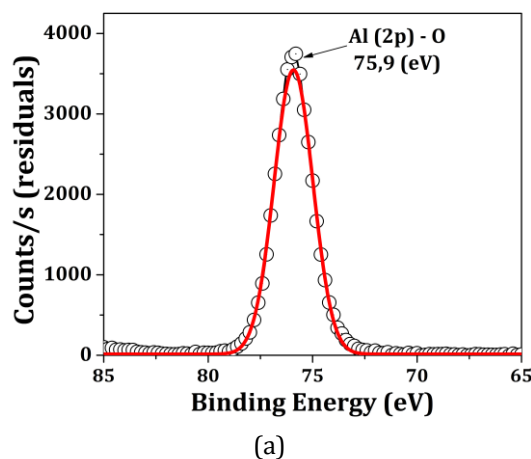


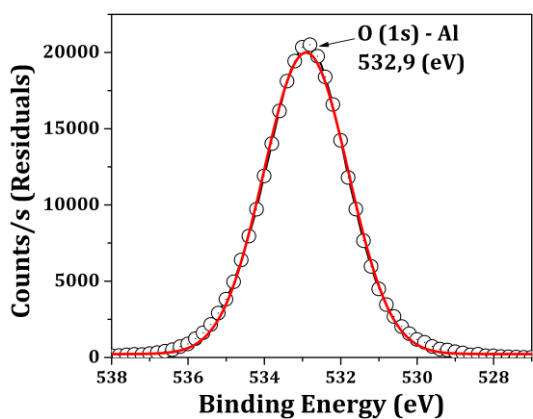
Fig. 3. Depth spectra obtained by the XPS technique for: (a) Al_2O_3 and (b) Si_3N_4 .

Fig. 3a shows the spectrum by XPS of the individual Al_2O_3 coating. It shows the presence of aluminum and oxygen with the presence of species such as Al-2s, Al-2p and O-1s. For a more complete analysis, Figs. 4a and 4b show the high-resolution spectra for Al-2p and O-1s, respectively. The data were adjusted by Gaussian functions and the quantitative analysis of the oxygen-aluminum ratio was carried out by calculating the area ratios at the peaks of the O-1s and Al-2p bands. The Al-2s peak at 121.09 eV and the presence of the carbon peak in coating at 284.5 eV were attributed to atmospheric contamination before the substrates entered the chamber (Fig.3a) [21]. The single layer Al_2O_3 coating is rich in oxygen with an atomic O/Al ratio of 1.77 ($\text{Al}_{64}\text{O}_{36}$ stoichiometry) very close to

the ideal atomic ratio (1.5) [21]. The adjustment of the high-resolution spectrum for the O-1s shown in Fig. 4b indicates only one prominent wide peak which is centered at 532.9 eV and is attributed to the Al-O link in the structure of the $\alpha\text{-Al}_2\text{O}_3$ [22]. The presence of the Al-2p peak at the 75.9 eV position indicates that the aluminum present in the surface region is found as Al_2O_3 . In addition, the Al-2p peak in Fig. 4a was adjusted with only one individual peak, showing that indeed the aluminum present in the layer is completely oxidized in the Al_2O_3 form as reported by other authors [23].

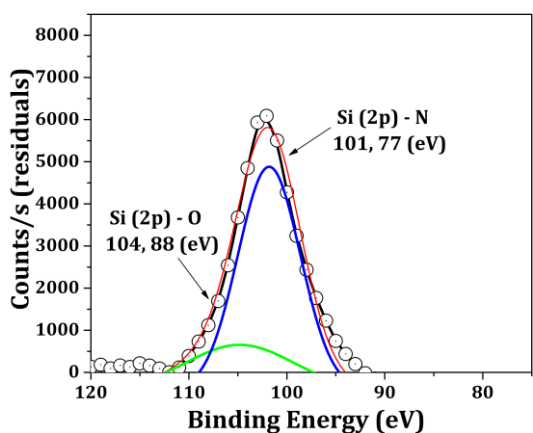
Fig. 3b shows the XPS spectrum of the single layer Si_3N_4 coating. From this spectrum, it was found that in addition to the Si and N elements, the layer has little amount of O. In order to know the detailed surface stoichiometry of the coating, the high resolution XPS spectra of the Si-2p and N-1s species are also presented in Fig. 5a and 5b, respectively. The single layer coating of Si_3N_4 has an atomic N/Si ratio of 1.32 (Stoichiometry $\text{Si}_{57}\text{N}_{43}$). The Si_3N_4 has an ideal stoichiometry ratio of 1.33 which is in line with what was found. The high-resolution Si-2p spectrum (Fig. 5a) consists of two peaks located at a bond energy of 101.77 eV and 104.88 eV, respectively. These two peaks have been observed by other researchers and are assigned to the Si-O and Si-N links of the Si_3N_4 [24]. In contrast, the high-resolution spectrum of N-1s (Fig. 5b) is broken down into three peaks, the first located at 400.51 eV which corresponds to the N-O bond [25], the second located at a bond energy of 396.96 eV corresponding to the N-Si bond, and the third located at a bond energy of 394.4 eV which can be attributed to a different chemical state of N due to its different bonding configurations with neighboring atoms such as H and C [26].



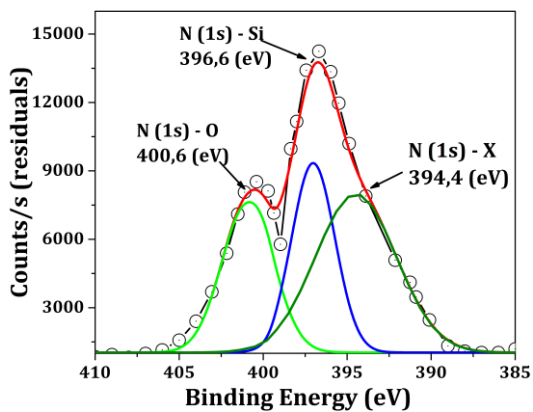


(b)

Fig. 4. High resolution XPS spectra for the Al_2O_3 coating: (a) $Al-2p$ signal; (b) $O-1s$ signal.



(a)



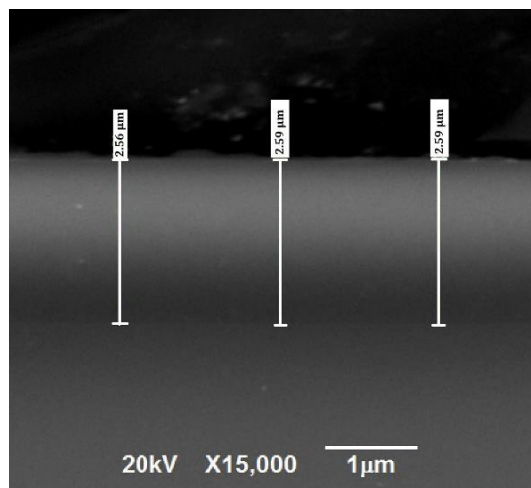
(b)

Fig. 5. High resolution XPS spectra for the Si_3N_4 coating: (a) $Si-2p$ signal; (b) $N-1s$ signal.

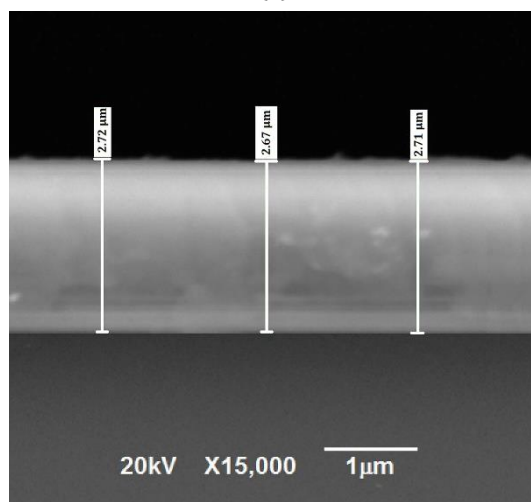
3.3 Scanning electron microscopy (SEM)

Figs. 6a and 6b show the micrographs obtained by scanning electron microscopy (SEM) of the cross section of the Al_2O_3 and Si_3N_4 coatings, respectively, deposited on silicon substrates (100). The corresponding thicknesses were determined for each coating, obtaining a

thickness of around $2.58 \pm 0.12 \mu m$ for the Al_2O_3 coating and $2.54 \pm 0.13 \mu m$ for the Si_3N_4 coating. The micrographs show a significant difference in the shade of the coatings, being the Si_3N_4 coating the brightest shade and the Al_2O_3 coating the darkest shade. This shade change is produced by the electronic density of each coating. On the other hand, the reduction of columnar growth is attributed to a high ion bombardment of Ar^+ atoms (Bias voltage), generating a highly dense cross section.



(a)



(b)

Fig. 6. SEM micrograph of the cross-section for the (a) Al_2O_3 coating and (b) Si_3N_4 coating.

3.4 Surface analysis

3.4.1 Atomic force microscopy

Figure 7 presents the AFM images for both coatings, where it was determined that both coatings presented a circular grain morphology and the Si_3N_4 coating presented a smaller grain

size and a more homogeneous surface compared to the Al_2O_3 coating. This homogeneous surface is attributed to a high ion bombardment of Ar^+ atoms (Bias voltage) generated during the deposition process, modifying the surface morphology of the layers. This bombardment causes an increase of the energy of the adsorbed atoms on the surface of the substrate, generating an increase of the nucleation sites and thus reducing the grain size, roughness and columnar growth, as well as an increase in the density of the coatings [27, 28].

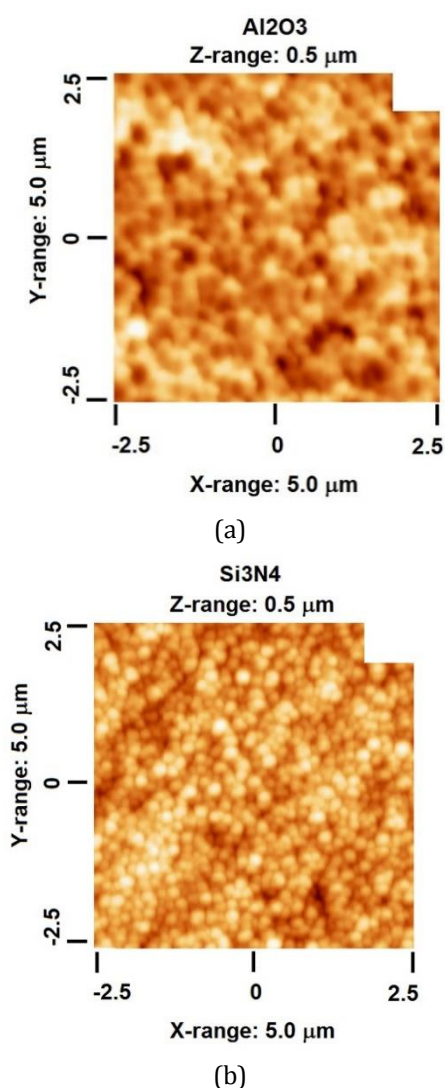


Fig. 7. Atomic force microscopy (AFM) images for the single layer (a) Al_2O_3 and (b) Si_3N_4 coatings.

Figures 8a and 8b present the roughness and grain size analysis for all the coatings, where it was determined that the Si_3N_4 coating presented a roughness reduction of 26.78% and a grain size reduction of 17.48% in relation to the Al_2O_3 coating. It was thus determined that the surface

of Si_3N_4 presented a greater quantity of grains in a certain area generating a greater density of grain boundaries, being these grain boundaries obstacles or impediments to the movement of dislocations, which influences the mechanical properties. Therefore, these morphological characteristics affect the mechanical and tribological properties of the coatings.

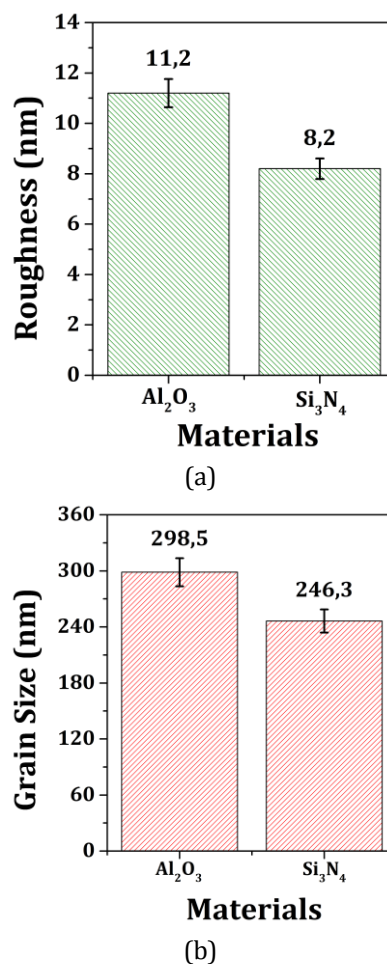


Fig. 8. Morphological analysis of the Al_2O_3 and Si_3N_4 coatings: (a) Roughness and (b) grain size.

3.5 Mechanical properties

Figure 9 shows the load-depth curves obtained from the nanoindentation tests for both coatings. In the graphs, the physical response of the surfaces is observed, showing that the Si_3N_4 coating presented a decrease in penetration of 38.7% in relation to the Al_2O_3 coating. This behavior is attributed to the hardness presented by this surface causing a higher resistance to be penetrated. The mechanical properties such as hardness (H) and modulus of elasticity (E) were studied using the Oliver and Pharr method [27].

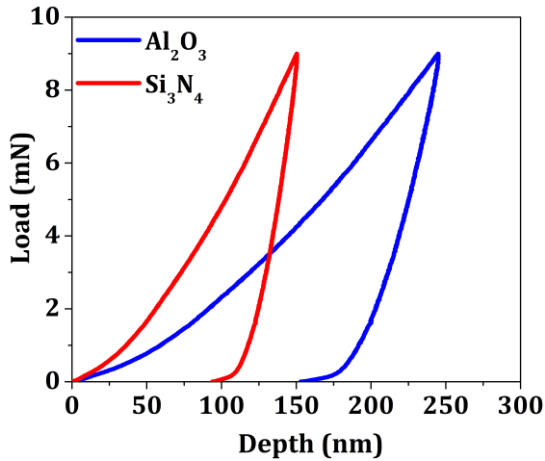


Fig. 9. Load-depth curves for the Al_2O_3 and Si_3N_4 coatings.

Figure 10 present the results of hardness (H) and reduced modulus of elasticity (E_r) of the coatings deposited on the AISI 316 steel substrates, respectively. It could be determined that the Si_3N_4 coating presented a greater resistance to being indented in comparison to the Al_2O_3 coating, this behavior is attributed to factors such as a smaller grain size (Fig. 8), which means that there was a greater amount of grain boundaries, which acted as impediments or obstacles to the sliding of the dislocations, therefore, a greater amount of energy was required to overcome these obstacles [29]. In addition, the compressive stress generated during the deposition process contributed to the increase of the hardness; therefore, the Si_3N_4 layer provided better mechanical properties such as hardness (H) and reduced modulus of elasticity (E_r).

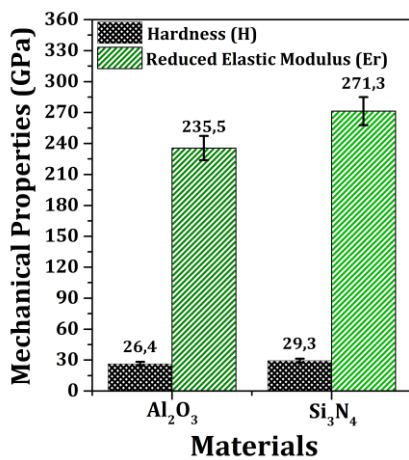


Fig. 10. Mechanical properties as a function of the material: Hardness and reduced modulus of elasticity for the Al_2O_3 and Si_3N_4 coatings.

From the results of nanoindentation, the resistance to plastic deformation (H^3/E^2) and the elastic recovery (R) were determined. The elastic recovery of the coatings was calculated by means of the following equation [30]:

$$R = \frac{\delta_{max} - \delta_p}{\delta_{max}} \quad (6)$$

Where δ_{max} is the maximum displacement and δ_p is the residual displacement. The data for Eq. 6 was taken from the load-depth curves presented in Figure 9. Figures 11a and 11b show the values obtained for plastic deformation resistance (H^3/E^2) and elastic recovery (R) for both coatings. It was determined that the highest resistance to plastic deformation (H^3/E^2) and elastic recovery (R) was obtained by the Si_3N_4 coating, which is mainly due to its mechanical properties such as hardness and reduced modulus of elasticity, analyzed previously.

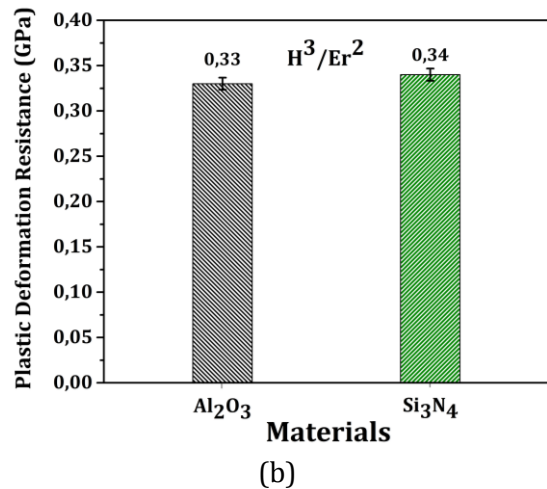
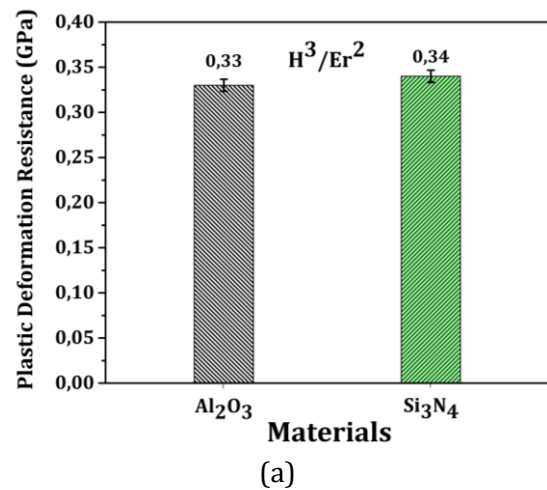


Fig. 11. Mechanical properties: (a) Resistance to plastic deformation and (b) elastic recovery of the Al_2O_3 and Si_3N_4 coatings.

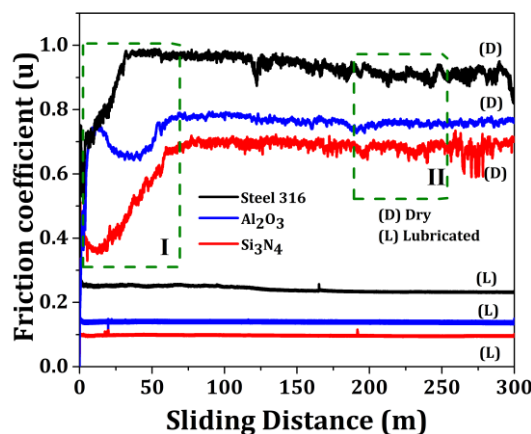
3.6 Tribological Pin-On Disk wear test

Figure 12a shows the friction coefficient of the tribological pair between the steel pin (100Cr6) and the surface of the Al₂O₃ and Si₃N₄ coatings deposited on the AISI 316 steel substrates, in a lubricated and non-lubricated environment. The friction results in dry environment present two characteristic stages, typical of the Pin-On-Disk test. Stage I, known as the start-up period, is associated with the interferential friction mechanism due to the contact of the asperities and the counterpart (100Cr6 steel pin), in which the asperities are reduced, leading to the formation of wear particles or debris [27], these particles on the surface generate a rapid increase in the friction coefficient followed by a slight decrease until it is stabilized. In stage II, the reduction of such asperities is maintained together with the appearance of new defects in the coating, which leads to a stabilization of such friction coefficient [31]. In the lubricated environment, the curves show a completely different behavior compared to the dry (non-lubricated) environment, since the introduction of the lubricant within the tribological pair generated a great decrease in the friction coefficient on all surfaces. Therefore, the change in the friction coefficient is due to the fact that the lubricant was able to support the external load exerted by the counterpart, decreasing the reduction of roughness and generating a smaller amount of wear particles (debris) on the surface of the tribo-system.

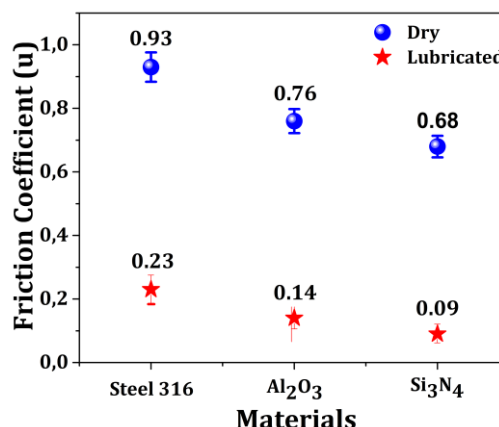
Fig. 12b shows the value of the friction coefficient of the tribological pair as a function of the material, in the dry and lubricated environment. This behavior is related to the friction model proposed by Archard [32]. The model correlates the mechanical properties (*H*, *E_r*) and morphological properties (roughness) of the coatings (Eq. 7), where it is indicated that the surfaces with better mechanical properties and lower roughness will present a lower coefficient of friction, as was the case of the Si₃N₄ coating tested in the tribological test. This is due to the fact that the surface of the Si₃N₄ coating is able to support the continuous passage of the counterpart in relation to the uncoated steel substrate and the Al₂O₃ coating, thus producing a lower wear rate on its surface.

$$\mu = \frac{F_f}{F_n} = C_k \frac{R_{(s,a)}}{\sigma t_{(H,E_r)}} \quad (7)$$

Where μ is the friction coefficient of the system, C_k is an adjustment constant that depends on the test conditions, $R_{(s,a)}$ is the roughness of the coating which can be quadratic or arithmetic and $\sigma t_{(H,E_r)}$ is a variable that depends on the mechanical properties of the system such as hardness (*H*) or modulus of elasticity (*E_r*).



(a)



(b)

Fig. 12. Tribological properties of the Al₂O₃ and Si₃N₄ coatings in non-lubricated and lubricated environment: (a) Friction coefficient as a function of sliding distance from the Pin-on-Disk test and (b) Friction coefficient as a function of the material evaluated.

Fig. 13 shows the 3D profiles of the wear tracks, which allow the corroboration of the tribological test results presented in Figs. 12a and 12b, where the wear on all three surfaces is displayed, uncoated 316 steel, 316 steel/ Al₂O₃ and 316 steel/Si₃N₄, in a dry and lubricated environment. In the dry environment, it was evidenced that the Si₃N₄ layer presented a

smaller amplitude and penetration of the wear track. This was due to its mechanical and morphological properties in comparison to the other surfaces, which corroborates the results previously presented. In a lubricated environment, the surface of the 316 steel substrate, shown in Fig. 13d, shows greater wear on the surface, due to the fact that the

addition of the lubricant in the tribological pair was not able to support all the load exerted by the counterpart during the tribological test, and that such surface had low mechanical and morphological properties in relation to the other surfaces. On the other hand, there was less wear on the surfaces of the Al_2O_3 and Si_3N_4 coatings as shown in Figs. 13e and 13f.

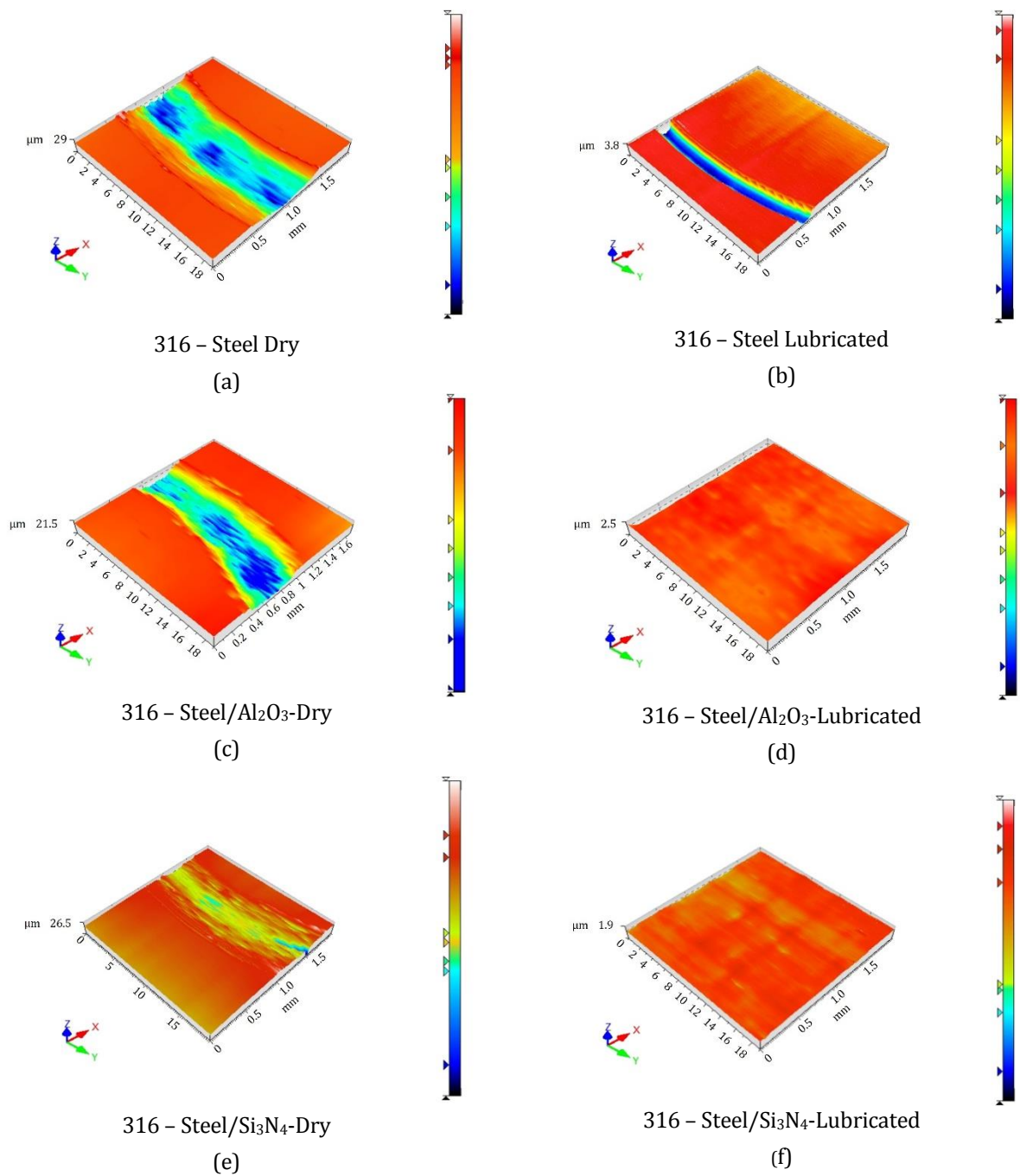


Fig. 13. Images of the 3D profiles for the wear tracks in dry and lubricated environment: (a) uncoated 316 stainless steel in dry environment, (b) uncoated 316 stainless steel in lubricated environment, (c) 316 steel/ Al_2O_3 in dry environment (d) 316 steel/ Al_2O_3 in lubricated environment, (e) 316 steel/ Si_3N_4 in dry environment, and (f) 316 steel/ Si_3N_4 in lubricated environment.

For a better analysis of the wear produced during the tribological test, a quantification of the wear rate for all the surfaces in dry and lubricated environment was made (Fig. 14), from the data obtained through Profilometry, calculated from the following equation [33]:

$$k = \frac{V}{F \times S} \quad (8)$$

Where k is the wear rate, F the applied force, V the track volume and S a factor dependent on the number of cycles or turns of the test

$$S = 2\pi rn \quad (9)$$

The results obtained on the wear rate for each surface are presented in Fig. 14, corroborating that the Si_3N_4 coating showed a higher wear resistance.

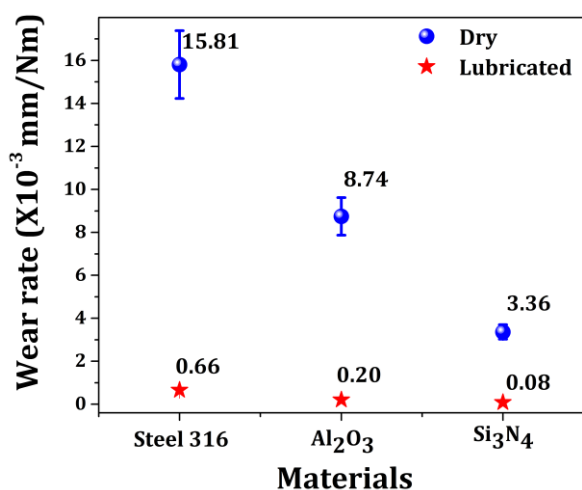


Fig. 14. Wear rate variation as a function of the material during tribological testing in dry and lubricated environment.

Figure 15 shows the SEM micrographs of all surfaces in a dry and lubricated environment in order to determine the wear mechanisms present on these surfaces. In the SEM micrographs, it was possible to observe an abrasive type of wear generated by the penetration and fracture of the asperities by the continuous passage of the counterpart on the surface, generating hardened abrasive particles by means of plastic deformation. These particles adhered to both surfaces in the tribological pair (counterpart - coating) generating a plowing and wear mechanism on that surface. It was also possible to observe a type of adhesive wear which was produced due to the fact that certain areas of the counterpart (steel pin) deformed plastically and adheres to the surface of

the coatings after supporting the external load exerted on the counterpart.

In the SEM micrographs of the wear tracks, it can be seen that for the uncoated 316 steel substrate in the dry environment (Fig. 15a), the predominant surface wear mechanisms were abrasives and adhesives. This was due to its low hardness and relatively high friction coefficient, which produced a large number of particles on the surface which were deformed and hardened by plastic deformation. In addition, the constant passage of the counterpart annihilated the asperities associated with the roughness and decreased the number of particles produced on the surface, generating micro-welding that later detach from the surface, producing material removal. For the uncoated 316 steel in the lubricated environment, there was a reduction in the friction coefficient and a reduction in wear (Fig. 15d), where only the presence of the plow mechanism was evident. This is attributed to the fact that the lubricant supported a great part of the external load produced by the counterpart, reducing in great quantity the number of abrasive particles on the surface, which produced a reduced wear on the surface.

On the surfaces of the Al_2O_3 and Si_3N_4 coated steel substrates in the dry environment (Figs. 15b and 15c), it was determined that the predominant wear mechanisms on these surfaces were adhesion and abrasion, although they were lower in relation to the uncoated steel. This change in behavior in relation to the 316 steel substrate is due to the change in mechanical properties and surface morphologies which provide a greater resistance to being deformed, producing a lower amount of material removal and wear. Additionally, the surfaces of the Al_2O_3 and Si_3N_4 coatings were analyzed in a lubricated environment (Figs. 15e and 15f) where it was evident that the surfaces presented very little wear. According to the grayscale, the formation of different types of oxides can be observed, starting with the natural oxides of the film (aluminum oxide) and the secondary oxides that are associated with the oxidation of the counterpart of the chrome pin. These oxides act as an intermediate substance that contributes to the reduction of friction, because they act as lubricants.

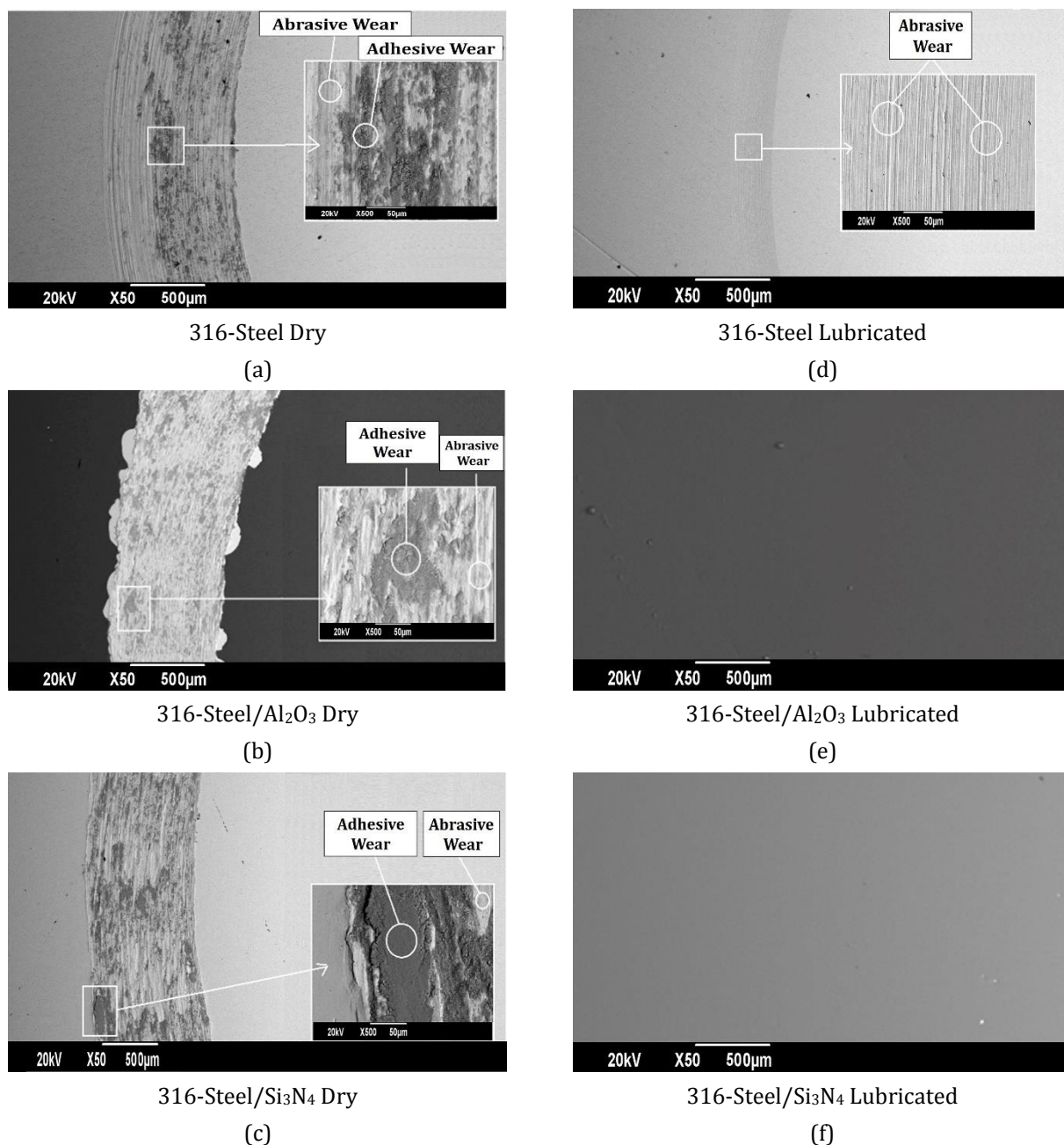


Fig. 15. SEM micrographs for wear tracks in dry and lubricated environments: (a) uncoated 316 stainless steel in dry environment, (b) 316 steel/ Al₂O₃ in dry environment, (c) 316 steel/ Si₃N₄ in dry environment, (d) uncoated 316 steel in lubricated environment, (e) 316 steel/ Al₂O₃ in lubricated environment and (f) 316 steel/ Si₃N₄ in lubricated environment.

3.7 Scratch test analysis

Figure 16 presents the critical load values for the Al₂O₃ and Si₃N₄ coatings, where the types of cohesive (L_{C1}) and adhesive (L_{C2}) failures were determined. In the cohesive failure (L_{C1}) the first cracks or failures are produced by the external load applied, and in the adhesive failure (L_{C2}) a delamination is generated at the edge of the scratching track. It was determined that in the Si₃N₄ coating, both types of failures (L_{C1} and L_{C2}) occur at

a higher load compared to the Al₂O₃ coating, indicating that a higher external load is required to produce the delamination of this coating, which is attributed to its mechanical and tribological properties.

Figs. 17a and 17b show the SEM micrographs of the scratching tracks of both coatings, where the loads (L_{C1} and L_{C2}) are presented from the data obtained from Fig. 16. For the Al₂O₃ coating, the first change of slope was found to be associated with a load of

9.5 N and a distance of 1.1 mm, which refers to the cohesive failure L_{C1} , known as wedging spallation. This is followed by the L_{C2} failure known as adhesive failure, associated with a load of 28.6 N and a distance of 1.9 mm, where there was a delamination at the edge of the track, as well as within it; a detachment inside the track started to occur. For the Si_3N_4 coating, the cohesive failure (L_{C1}) occurred at a load of 15.1 N and a distance of 1.6 mm, where a gross spallation appeared. After that, the adhesive failure (L_{C2}) was presented at a load of 45.3 N with a distance of 3.1 mm; however, the micrographs presented in Fig. 17b were not conclusive due to the large interferential spallation area, which did not allow a good observation of the scratch track [29].

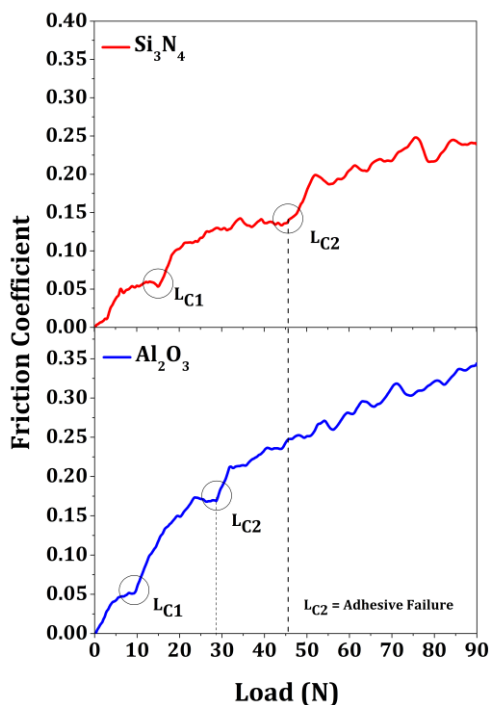


Fig. 16. Friction coefficient as a function of normal load for the Al_2O_3 and Si_3N_4 coatings.

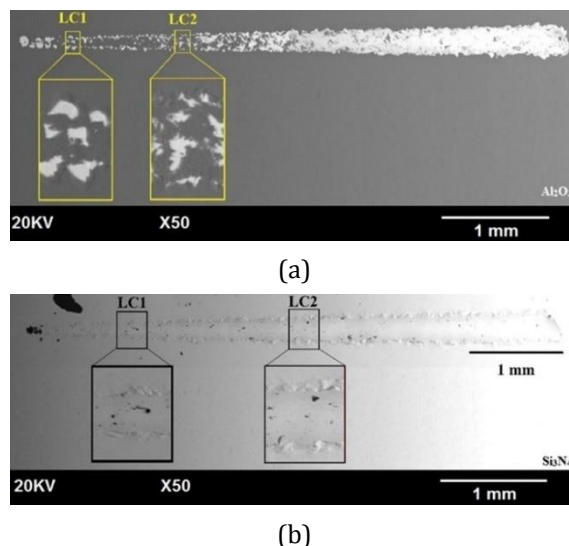


Fig. 17. SEM micrographs of the wear tracks generated in the scratch test for coatings deposited on 316 stainless steel substrates: (a) Al_2O_3 and (b) Si_3N_4 .

Figures 18a and 18b show a 45° top view of the 3D profiles of the scratch mark for the Al_2O_3 and Si_3N_4 coatings deposited on AISI 316 stainless steel substrates, respectively. It could be seen that as the indenter moved over the surface while increasing the load progressively, it generated a greater delamination and deformation on that surface. The evidence of this greater deformation is presented in the surroundings or edges of the scratching track (red areas), due to the displacement of material towards the edges and that it was more pronounced when the coating exceeds the critical load L_{C2} , (adhesive failure) where the detachment of the coatings began to occur. The critical load value is related to the mechanical (Figs. 9, 10 and 11) and tribological properties of the coatings (Figs. 12 and 13) and according to Figs. 16 and 17, the surface less affected by the critical load was the one corresponding to the Si_3N_4 coating, evidencing greater scratching resistance than the Al_2O_3 coating.

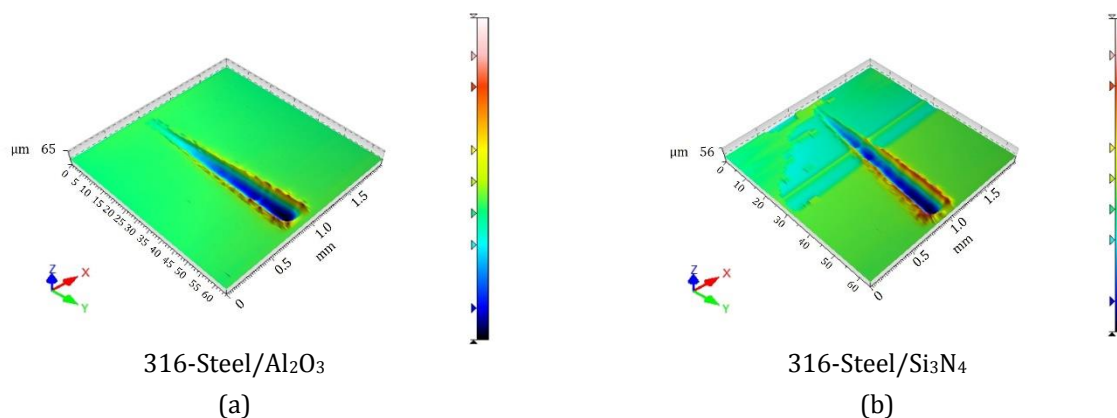


Fig. 18. Images of the 3D profiles of the wear tracks obtained from the Scratch test for the coatings deposited on AISI 316 stainless steel substrates: (a) Al_2O_3 and (b) Si_3N_4 .

CONCLUSIONS

By means of X-ray diffraction it was determined that the Al₂O₃ and Si₃N₄ coatings presented a Hexagonal and Cubic (FCC) structure, respectively. Additionally, it was found that the mismatch of the lattice parameters obtained experimentally in comparison with the international indexing charts for Al₂O₃ and Si₃N₄ were of 1.8% and 1.6%, respectively, due to residual stresses during the deposition process. By means of XPS, experimental stoichiometry relations of Al₃₆O₆₄ and Si₄₃N₅₇ were found, close to the ones found in literature.

AFM results showed that the Si₃N₄ coating had a smaller grain size relative to the Al₂O₃ coating, with a 17.45% decrease in grain size. Mechanical properties such as hardness (*H*) and modulus of elasticity (*E*) showed that the Si₃N₄ coating presented the best properties, with an increase of 9.9% and 13.19% for hardness and modulus of elasticity, respectively.

The tribological properties analyzed via Pin-On-Disk in dry and lubricated environment, determined that the Si₃N₄ coating presented the lowest friction coefficient and wear rate in relation to the Al₂O₃ coating. This behavior was attributed to its mechanical and morphological properties; therefore, the steel coated with Si₃N₄ showed to be the best option to be used as a protective coating in materials used in the food and pharmaceutical industries.

Acknowledgements

This research thanks the CDT-ASTIN SENA, regional Valle, Cali-Colombia; CINVESTAV, Mexico; Universitat de Barcelona, Catalunya, Spain; El centro de excelencia de nuevos materiales (CENM) of the Universidad del Valle in Colombia; to the project C.I 21024 of the Universidad del Valle for the funding.

REFERENCES

- [1] L. Fernandes, F. Silva, O. Paiva, A. Baptista, G. Pinto, *Minimizing the adhesion effects in food packages forming by the use of advanced coatings*, Procedia Manufacturing, vol.17, pp. 886-894, 2018, doi: [10.1016/j.promfg.2018.10.141](https://doi.org/10.1016/j.promfg.2018.10.141)
- [2] S.R. Werner, J.R. Jones, A.H. Paterson, R.H. Archer, D.L. Pearce, *Air-suspension coating in the food industry: Part II—micro-level process approach*, Powder Technology, vol. 171, iss. 1, pp. 34-45, 2007, doi: [10.1016/j.powtec.2006.08.015](https://doi.org/10.1016/j.powtec.2006.08.015)
- [3] M. Santamaria, G. Tranchida, F. Di Franco, *Corrosion Resistance of Passive Films on Different Stainless Steel Grades in Food and Beverage Industry*, Corrosion Science, vol. 173, pp. 1-12, 2020, doi: [10.1016/j.corsci.2020.108778](https://doi.org/10.1016/j.corsci.2020.108778)
- [4] M.R. De Figueiredo, M.D. Abad, A.J. Harris, C. Czettel, C. Mitterer, P. Hosemann, *Nanoindentation of chemical-vapor deposited Al2O3 hard coatings at elevated temperatures*, Thin Solid Films, vol. 578, pp. 20-24, 2015, doi: [10.1016/j.tsf.2015.01.069](https://doi.org/10.1016/j.tsf.2015.01.069)
- [5] D. Pakuła, L. Dobrzański, K. Gołombek, M. Pancielejko, A. Křiž, *Structure and properties of the Si3N4 nitride ceramics with hard wear resistant coatings*, Journal of materials processing technology, vol. 157-158, pp. 388-393, 2004, doi: [10.1016/j.jmatprotec.2004.09.060](https://doi.org/10.1016/j.jmatprotec.2004.09.060)
- [6] Y. Ou, X. Ouyang, B. Liao, X. Zhang, S. Zhang, *Hard yet tough CrN/Si3N4 multilayer coatings deposited by the combined deep oscillation magnetron sputtering and pulsed dc magnetron sputtering*, Applied Surface Science, vol. 502, 2020, doi: [10.1016/j.apsusc.2019.144168](https://doi.org/10.1016/j.apsusc.2019.144168)
- [7] E.T. Dominguez, P. Nguyen, A. Hylen, M.R. Maschmann, A. Mustapha, H. K. Hunt, *Design and characterization of mechanically stable, nanoporous TiO2 thin film antimicrobial coatings for food contact surfaces*, Materials Chemistry and Physics, vol. 251, pp. 1-13, 2020, doi: [10.1016/j.matchemphys.2020.123001](https://doi.org/10.1016/j.matchemphys.2020.123001)
- [8] A. Riedl, N. Schalk, C. Czettel, B. Sartory, C. Mitterer, *Tribological properties of Al2O3 hard coatings modified by mechanical blasting and polishing post-treatment*, Wear, vol. 289, pp. 9-16, 2012, doi: [10.1016/j.wear.2012.04.022](https://doi.org/10.1016/j.wear.2012.04.022)
- [9] C. Wang, Y. Lin, F. He, X. Luo, J. Tao, *Characterization of Al2O3 coatings oxidized from Al with different proportion of seed crystals at a lower temperature*, Applied Surface Science, vol. 283, pp. 87-93, 2013, doi: [10.1016/j.apsusc.2013.06.030](https://doi.org/10.1016/j.apsusc.2013.06.030)
- [10] K. Bobzin, *High-performance coatings for cutting tools*, CIRP Journal of Manufacturing Science and Technology, vol. 18, pp. 1-9, 2017, doi: [10.1016/j.cirpj.2016.11.004](https://doi.org/10.1016/j.cirpj.2016.11.004)
- [11] R. Manivannan, S. Sundararaj, R. Dheenasagar, K. Giridharan, P. Sivaraman, and V. Udhayarani, *Influence of Al2O3, SiC and B4C covalent multilayer PVD coating on surface properties of HSS rod*, Materials Today, Article in press, 2020, doi: [10.1016/j.matpr.2020.09.225](https://doi.org/10.1016/j.matpr.2020.09.225)

- [12] W. Liu, Q. Chu, J. Zeng, R. He, H. Wu, Z. Wu, S. Wu, *PVD-CrAlN and TiAlN coated Si3N4 ceramic cutting tools—1. Microstructure, turning performance and wear mechanism*, Ceramics International, vol. 43, iss. 12, pp. 8999-9004, 2017, doi: [10.1016/j.ceramint.2017.04.041](https://doi.org/10.1016/j.ceramint.2017.04.041)
- [13] W. Liu, Q. Chu, J. Zeng, R. He, H. Wu, Z. Wu, S. Wu, *PVD-CrAlN and TiAlN coated Si3N4 ceramic cutting inserts-2. High speed face milling performance and wear mechanism study*, Ceramics International, vol. 43, iss. 12, pp. 9488-9492, 2017, doi: [10.1016/j.ceramint.2017.04.127](https://doi.org/10.1016/j.ceramint.2017.04.127)
- [14] C. Abreu, M. Amaral, F. Oliveira, A. Tallaire, F. Benedic, O. Syll, R. Silva, *Tribological testing of self-mated nanocrystalline diamond coatings on Si3N4 ceramics*, Surface and Coatings Technology, vol. 200, iss. 22-23, pp. 6235-6239, 2006, doi: [10.1016/j.surfcoat.2005.11.071](https://doi.org/10.1016/j.surfcoat.2005.11.071)
- [15] I. Mohammadi, A. Afshar, S. Ahmadi, *Al2O3/Si3N4 nanocomposite coating on aluminum alloy by the anodizing route: Fabrication, characterization, mechanical properties and electrochemical behavior*, Ceramics International, vol. 42, iss. 10, pp. 12105-12114, 2016, doi: [10.1016/j.ceramint.2016.04.142](https://doi.org/10.1016/j.ceramint.2016.04.142)
- [16] ASTM G99, *Standard test method for wear testing with a pin-on-disk apparatus*, 2006,
- [17] ASTM G171, *Standard test method for scratch hardness of materials using a diamond stylus*, 2009.
- [18] M.L.R. García, A. J. González, *Rigaku DMAX 2200 X-ray Diffraction Equipment Basic Operation Manual*, Version 2006, Centro de Investigación en Energía Universidad Nacional Autónoma de México, 2006. (in Spanish)
- [19] J. Caicedo, G. Zambrano, W. Aperador, L. Escobar-Alarcon, E. Camps, *Mechanical and electrochemical characterization of vanadium nitride (VN) thin films*, Applied Surface Science, vol. 258, iss. 1, pp. 312-320, 2011, doi: [10.1016/j.apsusc.2011.08.057](https://doi.org/10.1016/j.apsusc.2011.08.057)
- [20] V. A. Thampi, A. Bendavid, B. Subramanian, *Nanostructured TiCrN thin films by Pulsed Magnetron Sputtering for cutting tool applications*, Ceramics International, vol. 42, iss. 8, pp. 9940-9948, 2016, doi: [10.1016/j.ceramint.2016.03.095](https://doi.org/10.1016/j.ceramint.2016.03.095)
- [21] S. Prasanna, G. Krishnendu, S. Shalini, P. Biji, G. M. Rao, S. Jayakumar, R. Balasundaraprabhu, *Composition, structure and electrical properties of DC reactive magnetron sputtered Al2O3 thin films*, Materials science in semiconductor processing, vol. 16, iss. 3, pp. 705-711, 2013, doi: [10.1016/j.mssp.2012.12.012](https://doi.org/10.1016/j.mssp.2012.12.012)
- [22] R. Prakash, S. Kumar, V. Kumar, R. Choudhary, D. Phase, *Optical and x-ray photoelectron spectroscopy studies of α -Al2O3*, AIP Conference Proceedings, vol. 1731, iss. 1, pp. 1-3, 2016, doi: [10.1063/1.4947751](https://doi.org/10.1063/1.4947751)
- [23] N. Rajopadhye, S. Dake, S. Bhoraskar, *Characterization of Al2O3 films deposited by various methods*, Thin Solid Films, vol. 142, iss. 1, pp. 127-138, 1986, doi: [10.1016/0040-6090\(86\)90308-1](https://doi.org/10.1016/0040-6090(86)90308-1)
- [24] H. Hu, A. Carim, *Determination of attenuation lengths and electron escape depths in silicon nitride thin films*, Journal of The Electrochemical Society, vol. 140, no. 11, 1993, doi: [10.1149/1.2221011](https://doi.org/10.1149/1.2221011)
- [25] K. Kishi, M. Roberts, *Adsorption of nitrogen and ammonia by polycrystalline iron surfaces in the temperature range 80–290 K studied by electron spectroscopy*, Surface Science, vol. 62, iss. 1, pp. 252-266, 1977, doi: [10.1016/0039-6028\(77\)90441-1](https://doi.org/10.1016/0039-6028(77)90441-1)
- [26] S.-H. Shin, J.-W. Cho, S.-H. Kim, *Structural investigations of CaO–CaF2–SiO2–Si3N4 based glasses by Raman spectroscopy and XPS considering its application to continuous casting of steels*, Materials & Design, vol. 76, pp. 1-8, 2015, doi: [10.1016/j.matdes.2015.03.035](https://doi.org/10.1016/j.matdes.2015.03.035)
- [27] C. Ortiz, H. Colorado, W. Aperador, A. Jurado, *Influence of the Number of Bilayers on the Mechanical and Tribological Properties in [TiN/TiCrN] n Multilayer Coatings Deposited by Magnetron Sputtering*, Tribology in industry, vol. 41, no. 3, pp.330-343, 2019, doi: [10.24874/ti.2019.41.03.03](https://doi.org/10.24874/ti.2019.41.03.03)
- [28] L. Ipaz, J. Caicedo, J. Esteve, F. Espinoza-Beltran, G. Zambrano, *Improvement of mechanical and tribological properties in steel surfaces by using titanium–aluminum/titanium–aluminum nitride multilayered system*, Applied Surface Science, vol. 258, iss. 8, pp. 3805-3814, 2012, doi: [10.1016/j.apsusc.2011.12.033](https://doi.org/10.1016/j.apsusc.2011.12.033)
- [29] V. Rodríguez, J. Caicedo, C. Amaya, C. Escobedo, G. Zambrano, F. Beltran, J. Muñoz-Saldaña, *The Evaluation of the Mechanical and Tribological Performance of Multilayers [Al2O3/YSZ] n Deposited on Silicon and AISI304 Steel Via Magnetron Sputtering*, vol. 40, no. 2, pp. 301-303, 2008. (in Spanish)
- [30] J. Archard, *Contact and rubbing of flat surfaces*. Journal of Applied physics, vol.24, iss. 8, pp. 981-988, 1953, doi: [10.1063/1.1721448](https://doi.org/10.1063/1.1721448)
- [31] W. Piedrahita, W. Aperador, J. Caicedo, P. Prieto, *Evolution of physical properties in hafnium carbonitride thin films*, Journal of Alloys and Compounds, vol. 690, pp. 485-496, 2017, doi: [10.1016/j.jallcom.2016.08.109](https://doi.org/10.1016/j.jallcom.2016.08.109)
- [32] H. O. Pierson, *Handbook of refractory carbides and nitrides: properties, characteristics, processing, and applications*, Noyes Publications. 1996,
- [33] J. Esteve, E. Martínez, A. Lousa, F. Montalá, L. Carreras, *Microtribological characterization of group V and VI metal-carbide wear-resistant coatings effective in the metal casting industry*, Surface and Coatings Technology, Vol. 133-134, pp. 314-318, 2000, doi: [10.1016/S0257-8972\(00\)00948-8](https://doi.org/10.1016/S0257-8972(00)00948-8)